



Article

Hyperspectral Marine Oil Spill Monitoring Using a Dual-Branch Spatial–Spectral Fusion Model

Junfang Yang ^{1,*} , Jian Wang ¹, Yabin Hu ², Yi Ma ², Zhongwei Li ¹ and Jie Zhang ^{1,2}

¹ College of Oceanography and Space Informatics, China University of Petroleum, Qingdao 266580, China; z20160058@s.upc.edu.cn (J.W.); lizhongwei@upc.edu.cn (Z.L.); zhangjie@upc.edu.cn (J.Z.)

² First Institute of Oceanography, Ministry of Natural Resources, Qingdao 266061, China; huyabin@fio.org.cn (Y.H.); mayimail@fio.org.cn (Y.M.)

* Correspondence: yangjunfang@upc.edu.cn; Tel.: +86-1786-422-9460

Abstract: Marine oil spills pose a crucial concern in the monitoring of marine environments, and optical remote sensing serves as a vital means for marine oil spill detection. However, optical remote sensing imagery is susceptible to interference from sunglints and shadows, leading to diminished spectral differences between oil films and seawater. This makes it challenging to accurately extract the boundaries of oil–water interfaces. To address these aforementioned issues, this paper proposes a model based on the graph convolutional architecture and spatial–spectral information fusion for the oil spill detection of real oil spill incidents. The model is experimentally evaluated using both spaceborne and airborne hyperspectral oil spill images. Research findings demonstrate the superior oil spill detection accuracy of the developed model when compared to Graph Convolutional Network (GCN) and CNN-Enhanced Graph Convolutional Network (CEGCN), across two hyperspectral datasets collected from the Bohai Sea. Moreover, the performance of the developed model in oil spill detection remains optimal, even with only 1% of the training samples. Similar conclusions are drawn from the oil spill hyperspectral data collected from the Yellow Sea. These results validate the efficacy and robustness of the proposed model for marine oil spill detection.

Keywords: marine oil spill detection; spatial–spectral fusion; deep learning; airborne hyperspectral image; spaceborne hyperspectral image



Citation: Yang, J.; Wang, J.; Hu, Y.; Ma, Y.; Li, Z.; Zhang, J. Hyperspectral Marine Oil Spill Monitoring Using a Dual-Branch Spatial–Spectral Fusion Model. *Remote Sens.* **2023**, *15*, 4170. <https://doi.org/10.3390/rs15174170>

Academic Editor: Merv Fingas

Received: 24 July 2023

Revised: 22 August 2023

Accepted: 23 August 2023

Published: 24 August 2023



Copyright: © 2023 by the authors. Licensee MDPI, Basel, Switzerland. This article is an open access article distributed under the terms and conditions of the Creative Commons Attribution (CC BY) license (<https://creativecommons.org/licenses/by/4.0/>).

1. Introduction

Marine oil spills are unforeseen events that arise from accidents or operational errors during the processes of petroleum exploration, development, and transportation, constituting the most emblematic and severe instances of marine environmental contamination. These spills pose significant threats to the marine environment, marine organisms, and human economic activities. Harmful substances can be transferred through the food chain, leading to long-term challenges in mitigating the resulting impacts [1–5]. Under suitable conditions, oil spills can also trigger harmful algal blooms, giving rise to more extensive ecological negative effects [6].

With the increasing demand for petroleum energy in China, the activities of offshore petroleum resource development, transportation, and storage are growing steadily, resulting in an escalating risk of offshore oil spills. As a major importer of crude oil, China relies on maritime transportation for 90% of its oil supply. In recent years, China has experienced frequent marine oil spill incidents. For instance, in 2010, an oil spill incident occurred as the result of an explosion in the Dalian Xingang oil pipeline. During 2011, there was an oil spill incident in the Penglai 19-3 oilfield [7]. Additionally, in 2013, an oil spill incident was caused by a leakage and explosion in the Sinopec pipeline at Huangdao [8,9]. The year 2018 witnessed an oil spill incident due to a collision involving the “SANCHI” tanker at the mouth of the Yangtze River [10,11]. Moreover, in 2019, an oil spill event transpired in

the vicinity of Dongsha Island in the South China Sea [12]. Following these occurrences, in 2021, another oil spill accident occurred on the oil platform in Penglai 19-3 oilfield. In the same year, the collision of the oil tanker “Symphony” at the Yangtze River Estuary caused an oil spill. The above events highlight the necessity and urgency of paying attention to the issue of oil spills [13]. According to statistic from the China’s State Oceanic Administration, there is an average of one oil spill incident occurring every four days along the coastal areas of China, with the provinces of Shandong and Guangdong being especially susceptible to such accidents [14].

The timely and accurate monitoring of the location and extent of marine oil spills, identification of oil types, and quantification of oil slick thickness play a crucial role in the emergency response to and effective disposal of marine oil spill incidents. Remote sensing, with its advantages of multi-source data, rapid data acquisition, and wide coverage, has become indispensable in emergency response and damage assessment related to marine oil spills [15–23]. In recent years, optical remote sensing techniques have been widely applied for monitoring oil spills on the sea surface [24–38]. Common optical remote sensing techniques include multispectral, hyperspectral, thermal infrared, ultraviolet, polarimetric, and LiDAR remote sensing. Among these, hyperspectral remote sensing, due to its higher spectral and spatial resolution, enables the extraction of subtle features between oil slicks and background seawater, as well as distinguishing different oil types. Consequently, it has found extensive applications in monitoring the location and distribution of oil spills [39–43], identifying oil types [44–48], and quantifying oil slick thickness [49–52].

However, the occurrence of marine oil spills is sudden, and optical remote sensing is susceptible to weather conditions, particularly disturbances caused by clouds, mist, and sunglints. These factors not only hinder the acquisition of optical images of marine oil spills, but also introduce confusion in the spectral and spatial information of oil slicks and seawater within the imagery, thus limiting the accuracy of marine oil spill detection. With the advancement of deep learning in image processing and classification, it has become possible to fully exploit the deep-level spectral and spatial features in images. This advancement enables effective suppression of the interference of clouds, mist, and sunglints, thereby showcasing immense potential in the field of marine oil spill detection. In response to the aforementioned challenges, some scholars have employed deep learning models based on spectral features for oil spill detection [53–55]. Although these methods have made certain progress, they have overlooked the importance of spatial information, such as the incomplete learning of edge information. Subsequently, many scholars have focused on the integration of spectral and spatial features, gradually developing models that combine both aspects, such as SSRN [56], DBMA [57], DBDA [58], ENL-FCN [59], etc. These models have been applied to marine oil spill detection by some researchers, yielding promising results [60–63].

Optical remote sensing images are susceptible to sunglints, which manifest as reduced spectral differences between oil slicks and seawater in the imagery and blurred spatial boundaries between them. Additionally, traditional convolutional networks can cause information loss during the feature extraction process. These factors significantly impact the accuracy of marine oil spill detection, particularly in accurately extracting the edge information of oil-water interfaces. In this study, a hyperspectral detection model for marine oil spills is developed based on the graph convolutional architecture, integrating the dual-branch spatial and spectral information. Then, the features extracted from the two branches are fused. Finally, experiments are conducted on both spaceborne and airborne oil spill hyperspectral images to validate the effectiveness of the proposed model for marine oil spill detection.

The main contributions of our study are mentioned as follows:

(1) For the extraction of spatial information, dilated convolutions are employed instead of standard convolutions, and a deep separable UNET network architecture is proposed to extract deep and shallow spatial features while enlarging the receptive field;

(2) For the extraction of spectral information, a residual graph convolution approach is designed, focusing on the spectral information of each layer and performing residual calculations to highlight the main spectral information;

(3) To evaluate the effect of the algorithm proposed in this study, we compared the oil spill detection results of spaceborne and airborne hyperspectral images based on the proposed method with other two graph convolutional network models. The proposed algorithm achieves best performance in marine oil spill detection.

2. Proposed Method

Due to the impact of sensor hardware, flight attitude, as well as clouds, wind, and waves, optical images of oil spills on the sea surface may suffer from some problems, such as bad lines, stripes, sunglints, and shadows, causing indistinct spectral differences between the oil film and the background seawater. To address these issues, this study constructs a model named Graph Convolutional–DS-UNET Neural Network (DUNET), which integrates dual-branch spatial and spectral information based on the graph convolutional architecture, for the detection of marine oil spills in the real oil spill incidents. The DUNET model consists of three main modules: spectral feature extraction, spatial feature extraction, and spatial–spectral feature fusion. The overall framework of DUNET is illustrated in Figure 1.

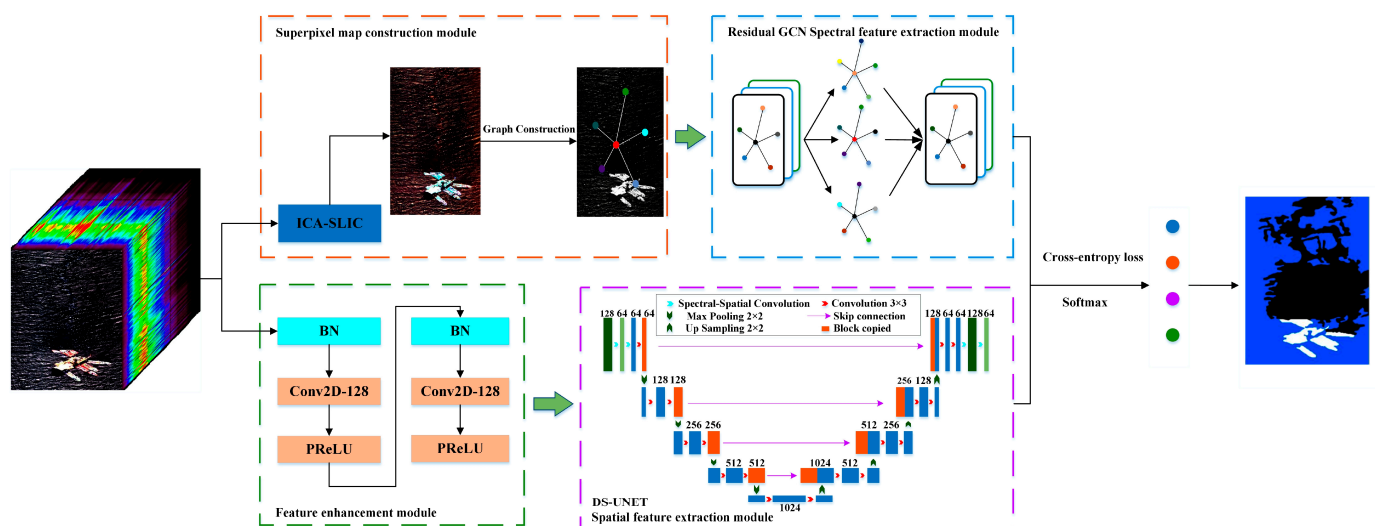


Figure 1. The architecture of the DUNET model for marine oil spill detection.

Firstly, linear iterative clustering is used to construct superpixel maps through continuous iteration; Afterwards, in the spectral branch, a residual Graph Convolutional Network (GCN) is used to extract spectral information. At the same time, in the spatial branch, feature enhancement modules are used to enhance the preprocessed images and remove redundancy; a deep separable UNET network is used to learn deep and shallow spatial information. Finally, the spectral features and spatial features of oil spills extracted from the two branches are fused, and the Cross Entropy loss function is used for optimization, so as to classify the finally extracted hyperspectral oil spill features.

2.1. Residual GCN Spectral Feature Extraction Module

The spectral feature extraction module designed based on GCN uses the spatial and spectral correlation between adjacent superpixel blocks to obtain the one to many relationship of features in the space by constructing a superpixel map. Assuming $G = (V, E)$, where V and E represent the vertex set and edge set, respectively. Therefore, we can define

the Adjacency matrix A , which defines the relationship of each point in the graph. Each element in the Adjacency matrix can usually be represented by Formula (1):

$$A_{i,j} = \exp\left(-\frac{\|x_i - x_j\|^2}{\sigma^2}\right), \quad (1)$$

where σ is the parameter that controls the width of the Radial Basis Function, and vector x_i, x_j represents the spectral characteristics related to vertices v_i and v_j . After A is calculated, the corresponding Laplacian matrix L can be solved, as shown in Formula (2).

$$L = I_N - D^{-\frac{1}{2}} A D^{-\frac{1}{2}}, \quad (2)$$

where I_N represents Identity matrix, and D represents Symmetric matrix of Adjacency matrix A , $D_{ii} = \sum_j A_{ij}$. More robust graph structure data can be obtained by normalizing the Laplace matrix. After a series of matrix changes, the expression for GCN is obtained as follows:

$$H^{(l)} = \sigma\left(\bar{A}^{(l-1)} W^{(l)}\right), \quad (3)$$

where $H^{(l)}$ represents the output of layer l , $\sigma(\cdot)$ represents the activation function, and W represents the weight.

In order to address the problem of gradient disappearance and overfitting caused by GCN, a residual GCN is proposed based on ResNet network structure. The expression is as follows:

$$H_{\text{Res}}^{(l+1)} = \sigma\left(\bar{A}^{(l)} W^{(l)}\right) + H^{(l)}, \quad (4)$$

The spectral feature information extracted by the residual GCN is named H_{spectral} .

2.2. Deep Separable U-Net Spatial Feature Extraction Module

The common network structure usually uses pooling layer to reduce the size of the image, so as to increase the receptive field relatively. However, in this process, some information will inevitably be lost. The advantage of the Dilated Convolution (or Expansion Convolution) algorithm is that it can expand the receptive field while avoiding information loss. It can retain the internal data structure and avoid the use of down sampling. It can also capture multi-scale context information by setting different expansion rates.

Depthwise Convolution and Pointwise Convolution can be combined to extract feature information from the Euclidean space of oil films. The number of feature maps after the Depthwise Convolution is the same as the number of channels in the input layer, making it impossible to extend the feature map. Moreover, it independently performs convolution operations on each channel in the input layer, which cannot effectively utilize the feature information of different channels in the same spatial position. Therefore, Pointwise Convolution is needed to combine these feature maps to generate new feature maps. The operation of Pointwise Convolution is very similar to conventional convolution operations, with a convolution kernel size of $1 \times 1 \times M$. M is the number of channels in the previous layer. Thus, the convolution operation here will weigh and combine the previous feature maps in the depth direction to generate new feature maps.

In this paper, DS-UNET is designed to make it more suitable for detecting marine oil spills by improving the U-Net network. Deep separable convolutions are introduced at the input and output ends, and dilated convolutions are introduced at the convolutional layer to achieve lightweight and reduce computational costs. The encoding module consists of two deep separable convolutional modules, two convolutional modules of 3×3 , and one the maximum pooling module of 2×2 . The decoding module is composed of one upsampling convolutional layer, concat feature concatenation, two convolutional modules of 3×3 , and two deep separable convolutional modules. Among them, deep separable convolution can reduce computational and parameter complexity. The structure of deep separable U-net network is shown in Figure 2.

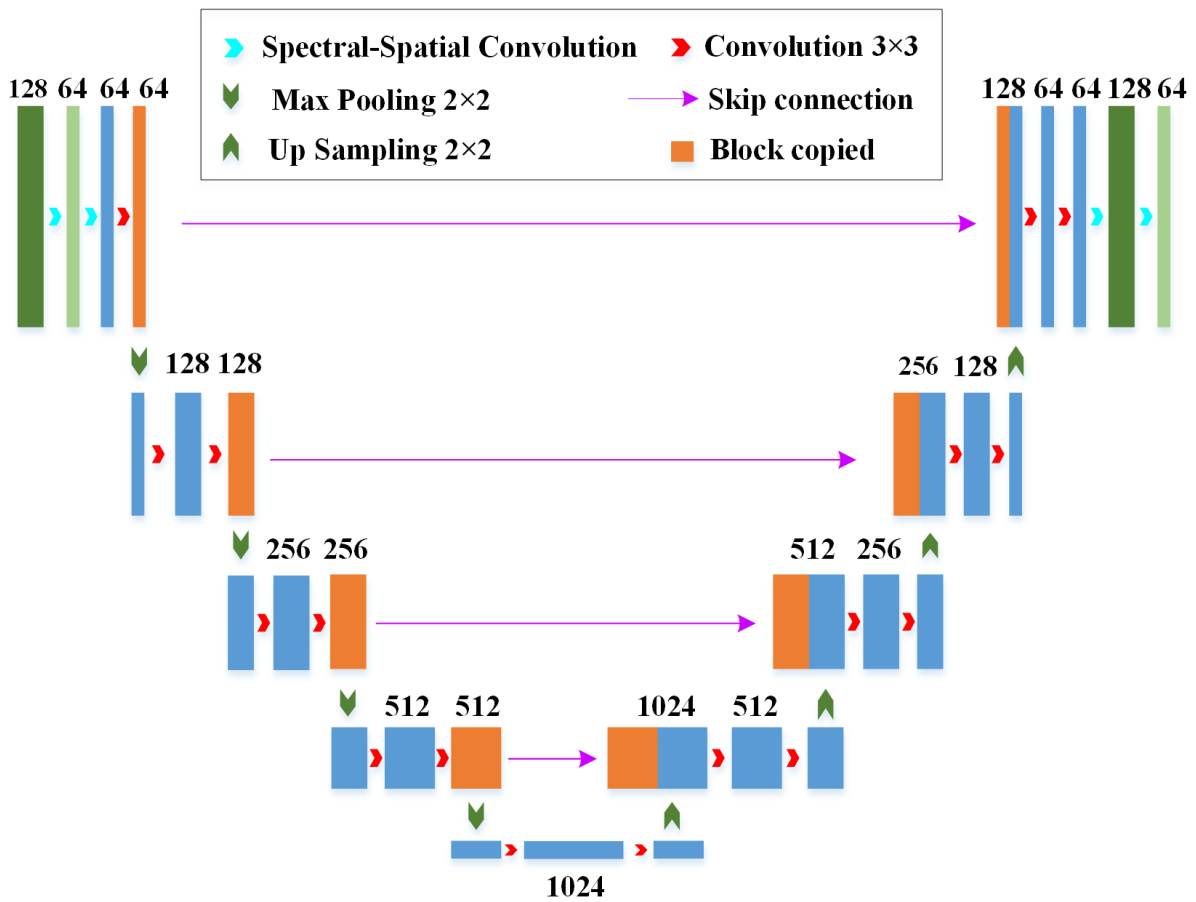


Figure 2. The structure of deep separable U-net network.

The output of the decoder is the deep and shallow spatial features extracted from the encoder, which are concatenated to fully extract the spatial information H_{spatial} of oil spills hyperspectral image.

2.3. Feature Fusion

The features obtained two branches are fused by feature concatenation, namely the spectral information obtained by the residual GCN spectral feature extraction module and the deep and shallow spatial information obtained by the deep separable U-Net spatial feature extraction module. Finally, the extracted oil film feature H (Formula (5)) is output. The eigenvectors are input into the softmax function, and final oil spill detection result is acquired through the Cross Entropy loss function, as shown in Formula (6).

$$H = H_{\text{spectral}} \cdot H_{\text{spatial}}, \quad (5)$$

$$L(Y, P) = -\frac{1}{N} \sum_{i=1}^N \sum_{c=1}^C y_{i,c} \log(p_{i,c}), \quad (6)$$

where Y represents the true value, P represents the predicted value of each pixel, and $y_{i,c}$ is the c -th element of label Y . $p_{i,c}$ represents the probability that pixel i belongs to class c , which is calculated using the softmax function. C and N represent the total number of categories and samples in the training dataset, respectively.

3. Results and Analysis

3.1. Data

The Bohai Sea, China's only inland sea, covers an area of 78,000 square kilometers, accounting for only 2.6% of China's marine territory. Due to its limited influence from ocean

currents and poor water exchange capacity, the Bohai Sea faces complex, high-intensity, and multiple sources of human activities. As a result, pollutants are difficult to purify rapidly, making it become a key area for monitoring pollutant emissions.

In this study, airborne hyperspectral imagery and spaceborne hyperspectral imagery obtained from two marine oil spill incidents in the Bohai Sea were selected as the data sources.

3.1.1. Hyperion Spaceborne Hyperspectral Data

The spaceborne hyperspectral imagery used in this study was Hyperion data acquired on 6 May 2007, in the Liaodong Bay of China (shown by the red pentagram in Figure 3). Hyperion is one of the three sensors mounted on the EO-1 satellite and is the first spaceborne civilian imaging spectrometer. The Hyperion imagery covers a spectral range of 400~2500 nm, spanning spectra from visible light to shortwave infrared, with a total of 242 spectral bands. The spectral resolution is 10 nm, and the spatial resolution is 30 m. Due to limitations in radiometric calibration and significant influence from water vapor and signal-to-noise ratio, only 175 bands (426~926 nm, 933~1346 nm, 1427~1810 nm, 1942~2385 nm) are actually usable in this study.

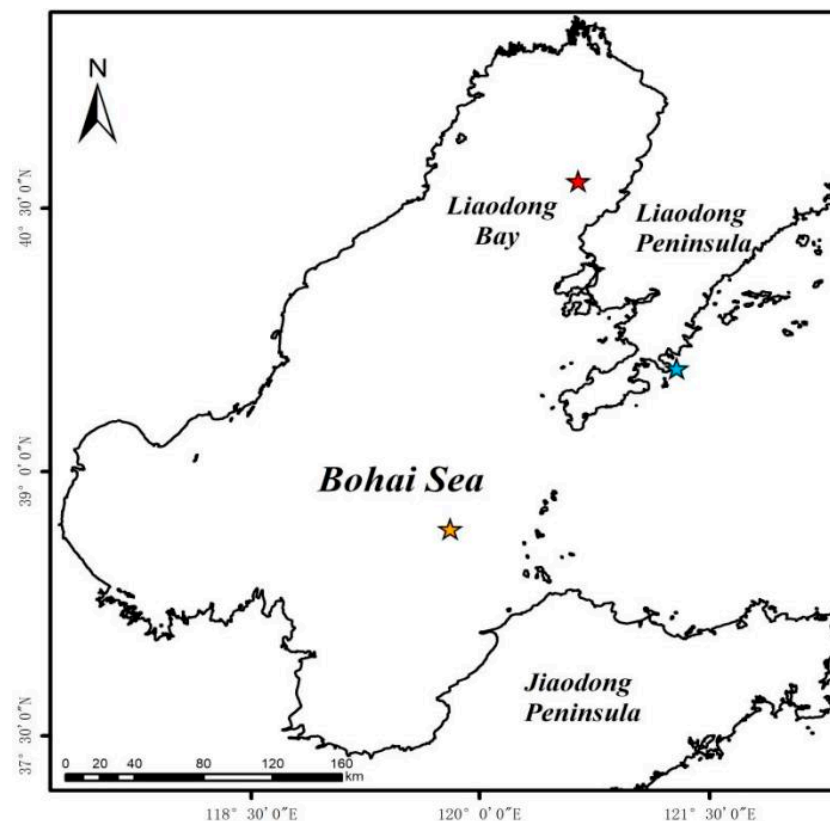


Figure 3. Distribution location of three oil spill accidents (the red pentagram represents the oil spill location of the Liaodong Bay in 2007, the orange pentagram represents the oil spill location of the Penglai 19-3 oilfield in 2011, and the blue pentagram represents the oil spill location of the Dalian Xingang in 2010).

The Hyperion imagery (Figure 4a) used in our experiments has dimensions of 444×400 pixels and contains information on oil slicks, seawater, and vessel tracks. However, the imagery also suffers from stripe noise and bad lines, severely affecting oil spill detection.

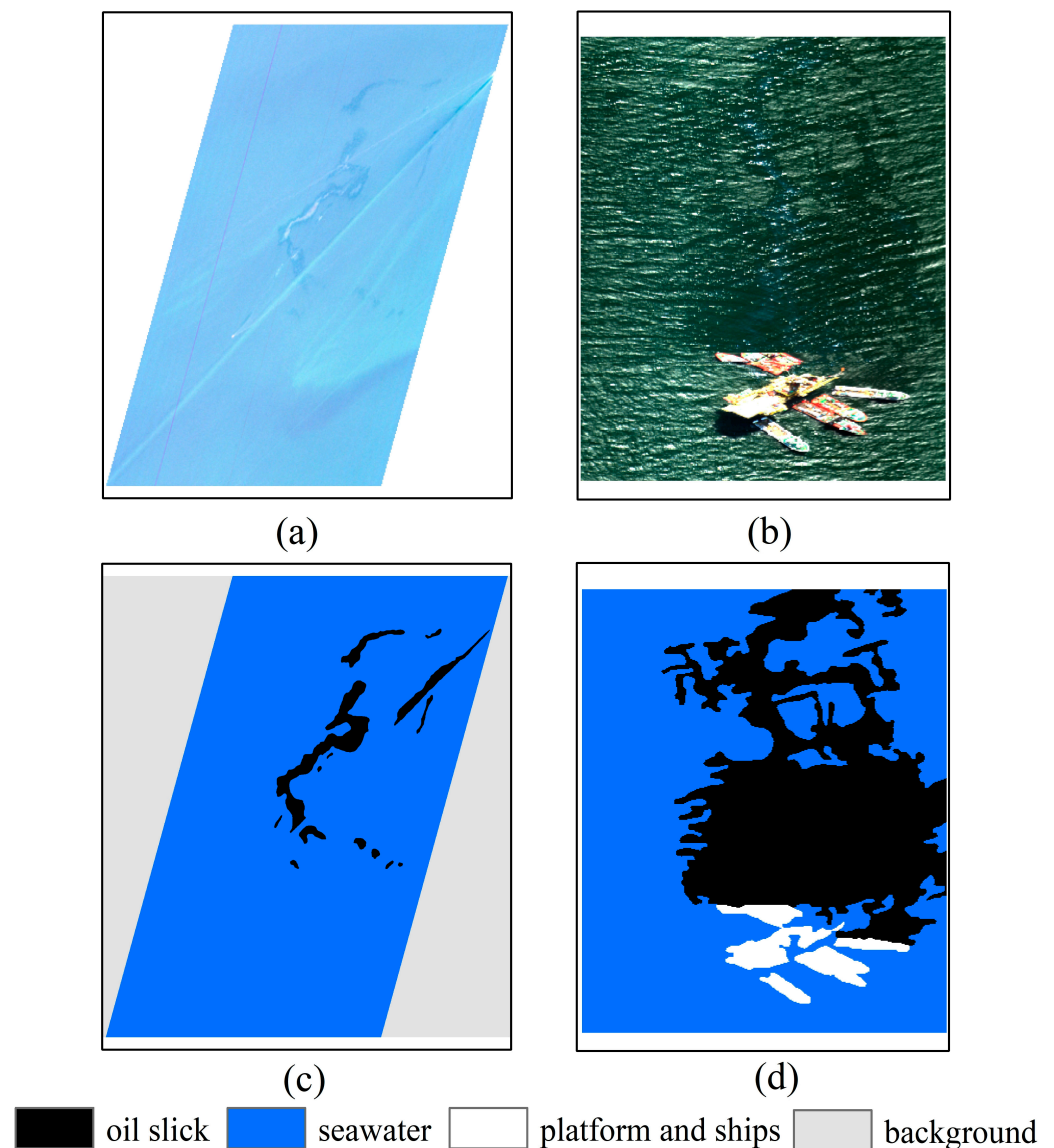


Figure 4. Hyperspectral oil spill images and corresponding ground truth images: (a) Hyperion spaceborne image in Liaodong Bay (R: 31, G: 20, B: 11); (b) AISA+ airborne image in Penglai 19-3 oilfield (R: 107, G: 68, B: 28); (c,d) the corresponding ground truth images.

3.1.2. AISA+ Airborne Hyperspectral Data

Unmanned aerial vehicles offer advantages such as high flexibility and strong real-time capabilities, compensating for the drawbacks of satellite remote sensing, such as lag and low accuracy. The airborne hyperspectral imagery used in this study was AISA+ data acquired by the China Marine Surveillance North Sea Aviation detachment on 23 August 2011, in the Penglai 19-3 oilfield (shown by the orange pentagram in Figure 3). The AISA+ imagery covers a spectral range of 400~970 nm, spanning the spectra from visible light to near-infrared, with a total of 258 spectral bands. The spectral resolution is 5 nm, and the sensor's field of view is 39.7° , with a spatial resolution of 1.41 m at a flying altitude of 1000 m. The AISA+ imagery (Figure 4b) used for oil spill detection in the Penglai 19-3 oilfield has dimensions of 444×364 pixels and was acquired at an approximate altitude of 700 m, with a spatial resolution of approximately 0.99 m. The imagery contains information on oil slicks, seawater, platform and ships. However, it is also affected by sunglints that can impact oil spill detection.

3.1.3. Ground Truth Data

The ground truth image of oil spill distribution for the Liao Dong Bay incident (Figure 4c) was produced through manual visual interpretation based on acquired hyperspectral images and expert knowledge. The ground truth image for the Penglai 19-3 oilfield incident (Figure 4d) was generated through manual visual interpretation based on a combination of on-site aerial photographs, hyperspectral images, and expert knowledge. Aerial photographs were taken using cameras mounted on Chinese Marine Surveillance aircraft, while the hyperspectral imagery was obtained synchronously using the AISA+ imaging spectrometer installed on Chinese Marine Surveillance aircraft. The ground truth image for the Liaodong Bay oil spill incident includes oil slicks seawater and background, while the ground truth image for the Penglai 19-3 oilfield incident includes oil slicks, seawater, platforms, and ships.

3.2. Experimental Setup

In this article, we randomly selected 5% of the samples for training, 5% for validation, and the remaining 90% for testing for each dataset. All experiments were performed on NVIDIA GeForce RTX 3090 GPU with 24 GB of memory (NVIDIA, Santa Clara, CA, USA). Table 1 lists the number of training, validation, and testing samples for the three datasets.

Table 1. Number of training, validation, and test samples in three datasets.

Dataset	Class	Training	Validation	Test	Total
Hyperion data in Liaodong Bay	Oil slick	219	219	3933	4371
	Seawater	5642	5642	101,561	112,845
	Background	3019	3019	54,346	60,384
AISA+ data in Penglai 19-3 oilfield	Oil slick	2691	2691	48,440	53,822
	Seawater	5083	5083	91,490	101,656
	Platform and ships	307	307	5524	6138

3.3. Experimental Results

The proposed method was applied to the two oil spill hyperspectral datasets, and two graph convolutional network models, including the GCN [64] and the CNN-Enhanced Graph Convolutional Network (CEGCN) [65], were selected for comparison. To ensure fairness in the comparative experiment, the three methods were evaluated using the same set of hyperparameters. The oil spill detection results of the proposed method and the other two algorithms on the two hyperspectral datasets are shown in Figure 5.

From Figure 5, it can be observed that there are differences in the oil spill detection capabilities between the proposed algorithm and the other two algorithms. The DUNET model achieves the closest results to the ground truth images for both datasets, with clear oil film boundaries and minimal misclassification. The CEGCN model performs slightly worse, with some oil films misclassified as seawater. The GCN model exhibits the largest differences from the ground truth images, particularly in terms of lacking attention to boundaries and details, as indicated by the dashed circles in Figure 5a,b. The detection results demonstrate the effectiveness of the DUNET model in utilizing both spatial and spectral information through dual branches and feature fusion to improve the detection results.

To quantitatively showcase the oil spill detection capabilities of the proposed model and the other two methods, four metrics were used for accuracy evaluation of the oil spill detection results, namely detection accuracy, overall accuracy, average accuracy, and the Kappa coefficient.

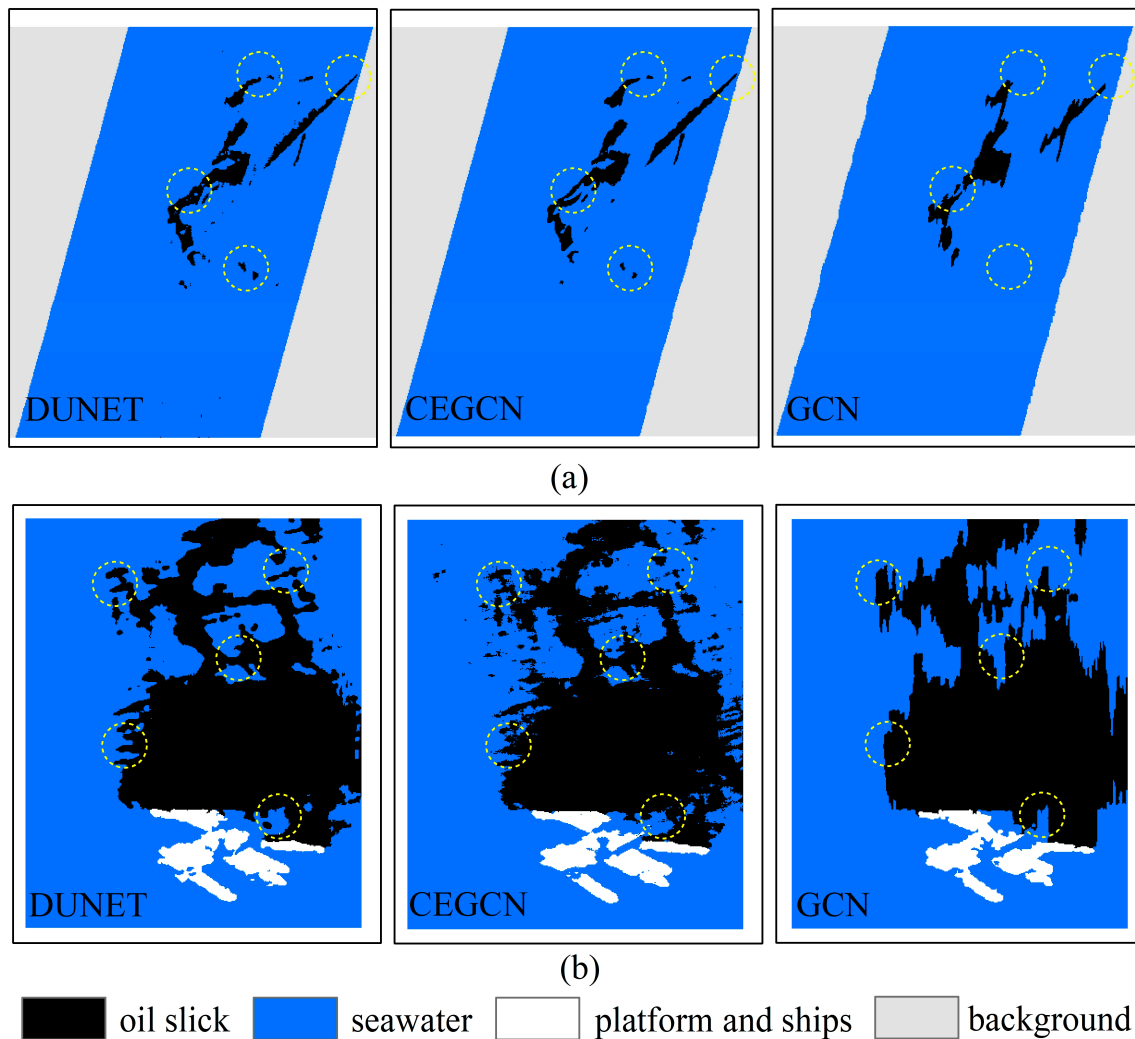


Figure 5. Oil spill detection results of DUNET, CEGCN, and GCN, based on different datasets: (a) Liaodong Bay dataset; (b) Penglai 19-3 oilfield dataset. Dashed circles represent the main differences between the classification results based on three models.

Overall, the DUNET model outperforms the CEGCN and GCN models in terms of oil spill detection accuracy, overall accuracy, average accuracy, and Kappa coefficient on two datasets (Table 2). Specifically, for the Hyperion dataset of Liaodong Bay, the DUNET model achieves an oil spill detection accuracy of 84.02%, which is 3.05% and 18.33% higher than that of the CEGCN and GCN models, respectively. The overall accuracy and average accuracy of the DUNET model are 99.17% and 94.42%, respectively, surpassing the CEGCN model by 0.62% and 1.05%, as well as the GCN model by 0.80% and 6.34%. As for the AISA+ dataset of the Penglai 19-3 oilfield, the DUNET model achieves an oil spill detection accuracy of 95.95%, and an improvement of 2.57% and 6.93% compared to the CEGCN and GCN models, respectively. The overall accuracy and average accuracy are 96.50% and 94.80%, surpassing the CEGCN model by 1.98% and 1.82%, as well as the GCN model by 4.92% and 5.52%. The Kappa coefficients of the DUNET model on two datasets are higher than 0.9, which are better than those of the CEGCN model and GCN model, indicating a strong agreement between the classification results of the DUNET model and the ground truth images. In summary, the proposed DUNET model achieves the best performance in oil spill detection compared to the CEGCN and GCN models.

Table 2. Oil spill detection accuracy of three algorithms based on different datasets.

Dataset	Class	DUNET	CEGCN	GCN
Hyperion data in Liaodong Bay	Oil slick	84.02	80.97	65.69
	Seawater	99.39	99.33	98.99
	Background	99.84	99.81	99.56
	Overall Accuracy (%)	99.17	98.55	98.37
	Average Accuracy (%)	94.42	93.37	88.08
	Kappa Coefficient	0.9826	0.9797	0.9658
AISA+ data in Penglai 19-3 oilfield	Oil slick	95.95	93.38	89.02
	Seawater	91.35	89.79	85.50
	Platform and ships	97.10	95.77	93.31
	Overall Accuracy (%)	96.50	94.52	91.58
	Average Accuracy (%)	94.80	92.98	89.28
	Kappa Coefficient	0.9009	0.8890	0.8288

4. Discussion

4.1. Impact of Different Proportions of Training Samples on Oil Spill Detection Performance

To further validate the robustness of the proposed model under different proportions of training samples, in this section, we randomly select 1%, 3%, and 5% of the training samples from the two datasets for model training. The oil spill detection results of the three methods based on different proportions of training samples are shown in Figure 6.

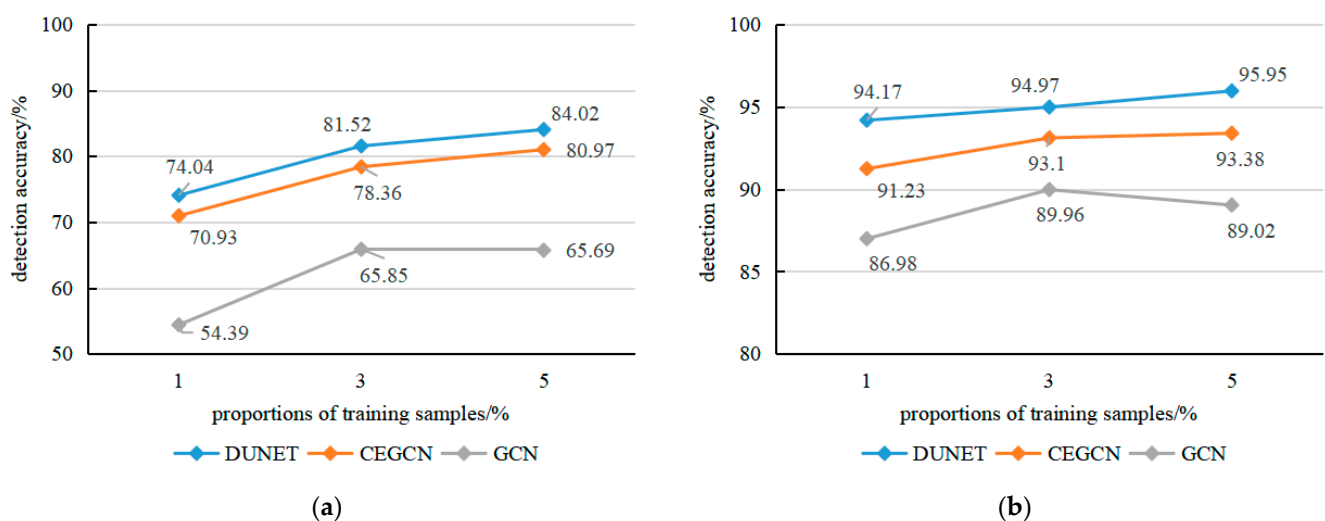


Figure 6. Oil spill detection accuracies of DUNET, CEGCN, and GCN, based on different proportions of training samples: (a) Liaodong Bay dataset; (b) Penglai 19-3 oilfield dataset.

Overall, the three methods exhibit different classification performance based on different proportions of training samples. For two hyperspectral datasets, as the proportion of training samples increases, the accuracy of oil spill detection for the three methods also gradually improves. However, the proposed DUNET method consistently achieves the highest detection accuracy, even under the condition of only 1% training samples, outperforming both CEGCN and GCN in oil film detection. At the same time, it can also be found that with the increasing proportion of training samples, the oil spill detection accuracy based on the fusion method of spatial and spectral information tends to stabilize, especially in the airborne AISA+ dataset. This could be attributed to the higher spectral and spatial resolution, as well as the larger dimensionality of the AISA+ data.

Furthermore, we conducted a comparison of the running times of DUNET, CEGCN, and GCN models under different proportions of training samples, as shown in Table 3. Overall, when considering the same proportion of training samples, the GCN model exhibited the shortest training time, followed by the CEGCN model, while the DUNET

model had a slightly longer training time. At the same time, the GCN model demonstrated the shortest test time, while the test times for the CEGCN and DUNET models were similar.

Table 3. Running time of three models under different proportions of training samples.

Dataset	Proportions Training Samples	DUNET		CEGCN		GCN	
		Training Time (s)	Test Time (s)	Training Time (s)	Test Time (s)	Training Time (s)	Test Time (s)
Hyperion data in Liaodong Bay	1%	50.64	11.15	40.79	12.23	34.79	10.67
	3%	50.84	10.71	41.87	13.25	34.84	10.73
	5%	55.57	15.56	39.65	11.09	34.84	10.87
AISA+ data in Penglai 19-3 oilfield	1%	57.43	16.87	42.42	14.47	38.5	14.36
	3%	54.43	14.52	42.36	14.7	49.51	25.95
	5%	55.38	15.82	42.41	14.41	38.42	14.63

4.2. Application on Oil Spill Image in the Yellow Sea

To further validate the effectiveness and applicability of the proposed method, in this section, we apply the developed model to AISA+ hyperspectral data that acquired at an oil spill incident in the Yellow Sea, namely the Dalian Xingang oil spill incident on 6 August 2010. The location of the oil spill image is indicated by the blue pentagram in Figure 3.

4.2.1. Oil Spill Detection Results

The AISA+ image (Figure 7a) used for the oil spill detection experiment in Dalian Xingang has dimensions of 256×384 pixels and contains information about both the oil slick and seawater. However, the image also contains striping and bad lines that can interfere the oil spill detection. A ground truth image of the oil spill distribution (Figure 7b) was created through the combination of aerial photographs and manual visual interpretation.

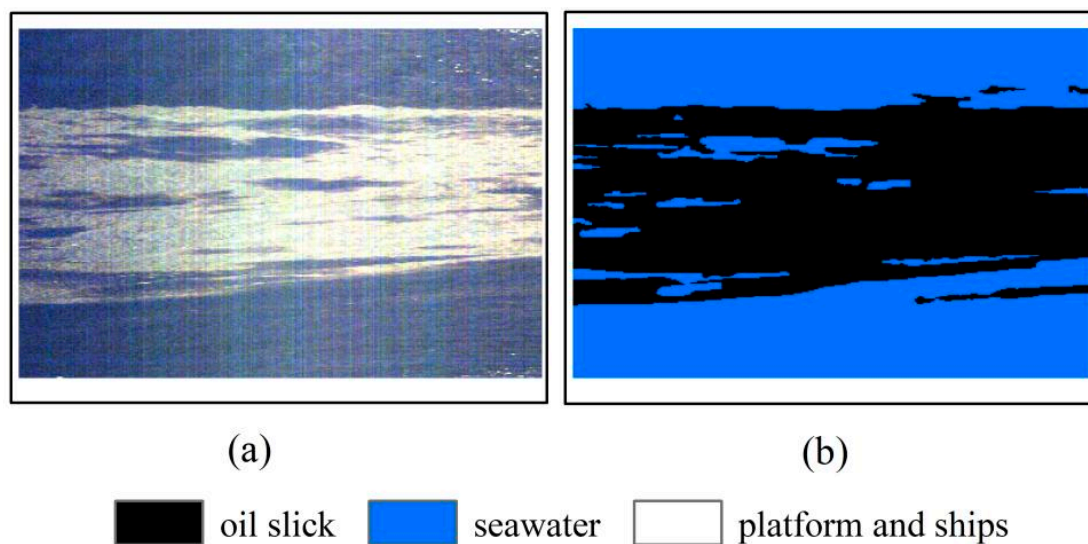


Figure 7. Hyperspectral oil spill image and corresponding ground truth image: (a) AISA+ airborne image in Dalian Xingang adjacent water (R: 107, G: 68, B: 28); (b) the corresponding ground truth image.

For the Dalian dataset, we randomly selected 5% of the samples for training, 5% for validation, and the remaining 90% for testing. Table 4 lists the number of training, validation, and testing samples for Dalian dataset.

We conducted oil spill detection experiments on AISA+ hyperspectral data in Dalian using the developed method and two other deep learning models, and the detection results are shown in Figure 8. Similar to the previous results, the oil spill detection results of the DUNET model are the closest to the ground truth image, with clear boundaries of the oil film and minimal misclassification. The CEGCN model performs slightly worse, with some

oil films being misclassified as seawater. The GCN model lacks attention to boundaries and fine details in the oil spill detection results, as shown in the dashed circle in Figure 8a–c.

Table 4. Number of training, validation, and test samples in the Dalian dataset.

Dataset	Class	Training	Validation	Test	Total
AISA+ data in Dalian	Oil slick	2349	2349	42,278	46,976
	Seawater	2566	2566	46,196	51,328

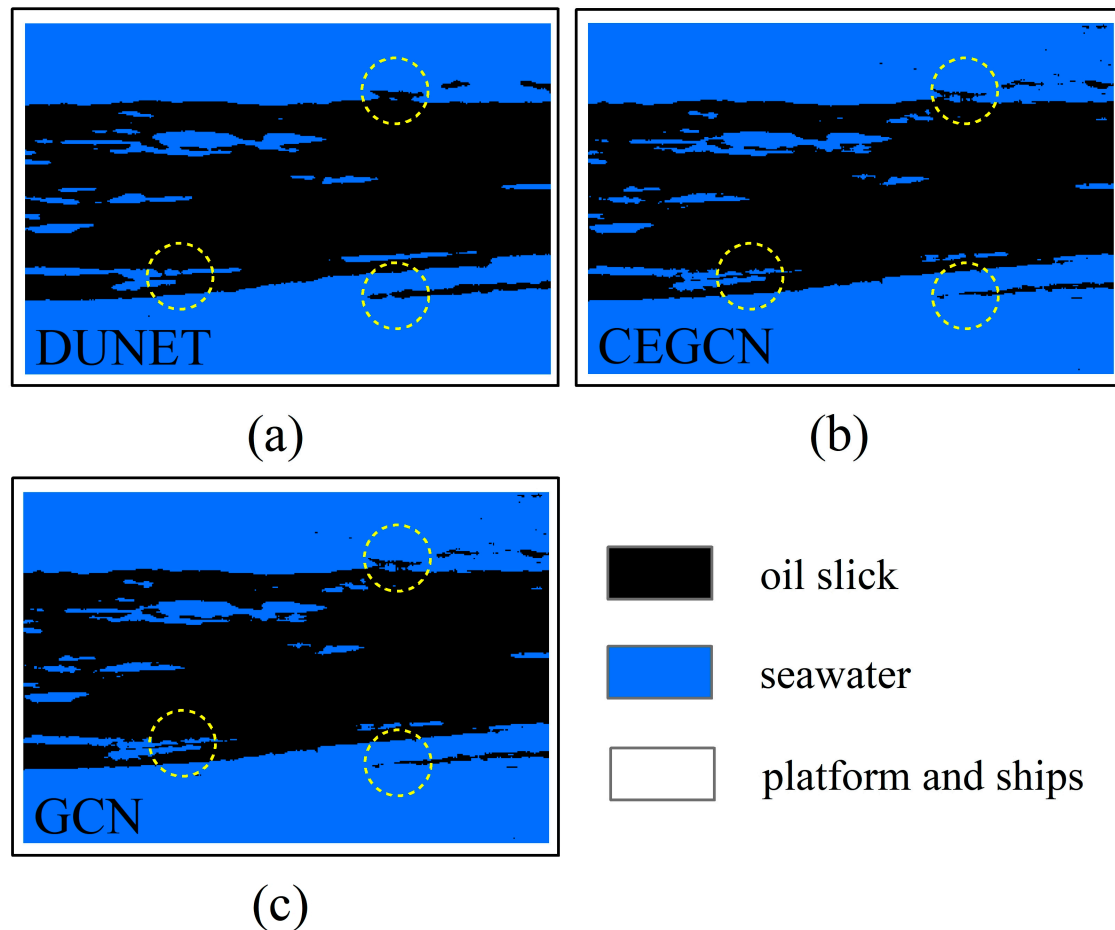


Figure 8. Oil spill detection results of three algorithms based on Dalian Xingang dataset: (a) DUNET; (b) CEGCN; (c) GCN. Dashed circles represent the main differences between the classification results based on three models.

In order to quantitatively demonstrate the oil spill detection capabilities of the proposed model and the other two methods, four indicators, namely detection accuracy, overall accuracy, average accuracy, and Kappa coefficient, were used to evaluate the accuracy of the oil spill detection results, as shown in Table 5.

Table 5. Oil spill detection accuracy of three algorithms based on the Dalian Xingang dataset.

Dataset	Class	DUNET	CEGCN	GCN
AISA+ data in Dalian	Oil slick	98.34	97.19	91.58
	Seawater	98.26	97.79	87.59
	Overall Accuracy (%)	98.30	97.50	89.50
	Average Accuracy (%)	98.30	97.49	89.59
	Kappa Coefficient	0.9659	0.9500	0.7899

Similar to the previous conclusions, the developed DUNET model achieves the highest accuracy, overall accuracy, average accuracy, and Kappa coefficient on the Dalian oil spill airborne hyperspectral dataset, followed by the CEGCN model, while the GCN model performs the worst. The DUNET model achieves an oil spill detection accuracy of 98.34% based on the Dalian AISA+ dataset, which is an improvement of 1.15% and 6.76% compared to the CEGCN and GCN models, respectively. The overall accuracy and average accuracy are both 98.30%, surpassing the CEGCN model by 0.80% and 0.81%, as well as the GCN model by 8.80% and 8.71%. The Kappa coefficient of DUNET model achieves 0.9659 based on the Dalian AISA+ dataset, outperforming the CEGCN and GCN models by 0.0159 and 0.1760, respectively. This demonstrates the applicability of the developed oil spill detection method in other marine areas, effectively detecting oil spills in hyperspectral images under the influence of striping. This indicates that the developed oil spill detection model is applicable to oil spill scenarios in other marine areas, effectively detecting oil spills in airborne hyperspectral images under striping effects.

4.2.2. Analysis of Different Proportions of Training Samples

To further validate the robustness of the proposed model under different proportions of training samples, in this section, we randomly select 1%, 3%, and 5% of the training samples from the Dalian oil spill dataset for model training. The oil spill detection results of the proposed model and the other two deep learning methods based on different proportions of training samples are shown in Figure 9.

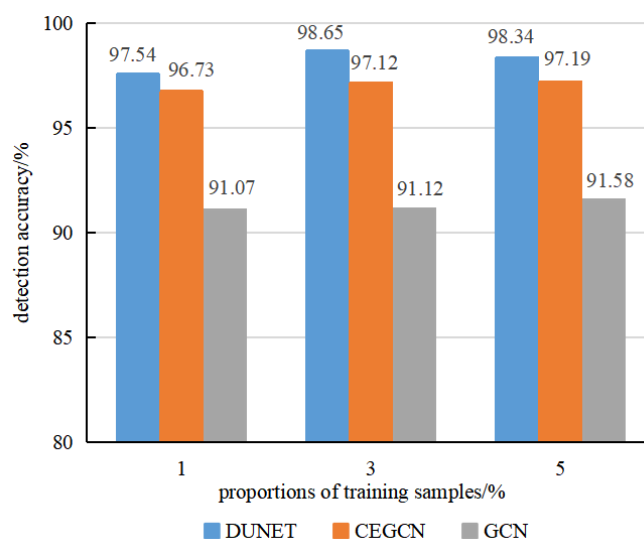


Figure 9. Oil spill detection accuracies of three algorithms based on different proportions of training samples from the Dalian Xingang dataset.

Overall, as the proportions of training samples increase, the oil spill detection accuracy of all three methods gradually improves. However, the proposed DUNET method consistently achieves the highest accuracy, even under the condition of only 1% training samples, outperforming both CEGCN and GCN in oil spill detection.

4.3. Analysis of Spectral Resolution of Sensor

Airborne hyperspectral sensors have high spatial and spectral resolution, strong maneuverability, and the ability to quickly respond to emergency situations, providing unparalleled advantages in obtaining timely information on marine oil spills. However, due to weather conditions and limited endurance, airborne hyperspectral data acquired is often scarce during oil spill incidents. On the other hand, spaceborne hyperspectral sensors have the advantage of continuously acquiring data consistently on a global scale.

However, they have lower spatial resolution, are prone to cloud interference, have long revisit periods, and lower signal-to-noise ratio.

The AISA+ airborne hyperspectral data used in this study has a spectral resolution of 5 nm and a spatial resolution of 0.99 m. The Hyperion spaceborne hyperspectral data has a spectral resolution of 10 nm and a spatial resolution of 30 m. Although Hyperion covers a wider spectral range, from 400 to 2500 nm, spanning visible light to shortwave infrared, compared to the spectral range of the AISA+ imagery (400~970 nm), it is worth noting that the oil spill detection accuracy based on AISA+ imagery consistently exceeds 90%, while the accuracy based on Hyperion imagery remains below 85%. This indicates that the oil spill detection accuracy based on AISA+ imagery, despite noticeable sunglint interference, is higher than that based on Hyperion imagery due to its higher spectral resolution. Furthermore, for data with higher spectral resolution, as the proportions of training samples gradually increase, the oil spill detection accuracy based on the spectral-spatial fusion method tends to stabilize.

5. Conclusions

China, as a major importer of crude oil, relies heavily on maritime transportation, with 90% of its crude oil imports being transported by sea. This inevitably increases the risk of marine oil spills. Timely and accurate monitoring of oil spill locations and extents plays a crucial role in effectively responding to and managing such unpredictable oil spill incidents. Hyperspectral remote sensing has been widely adopted for monitoring marine oil spills due to its superior spectral and spatial resolution capabilities. However, optical remote sensing images are susceptible to sunglints and shadows, which can reduce the spectral differences between oil films and seawater, especially in accurately extracting the edge information of oil-water interfaces. In light of these challenges, this study developed a GCN-based model that integrates spatial and spectral information from dual branches for hyperspectral oil spill detection in real marine scenarios.

The main conclusions drawn from this study are as follows: (1) Compared to the GCN and CEGCN, the proposed DUNET model achieved the best oil spill detection accuracy on two hyperspectral datasets from the Bohai Sea, confirming its effectiveness in hyperspectral oil spill detection. (2) The performance of the developed model in oil spill detection remains optimal, even with only 1% of the training samples, demonstrating its robustness. (3) When applied to hyperspectral oil spill data from the Yellow Sea, the developed model exhibited superior detection accuracy compared to the other two algorithms, further validating its applicability.

The findings highlight the effectiveness of the proposed model in different datasets and different proportions of training samples, emphasizing its potential significance in supporting oil spill monitoring and emergency response efforts in marine environments.

Author Contributions: Conceptualization, J.Y. and Y.H.; methodology, J.W. and J.Y.; software, J.Y. and J.W.; validation, J.Y. and J.W.; formal analysis, J.Y. and Y.H.; data curation, J.Y.; writing—original draft preparation, J.Y. and J.W.; writing—review and editing, J.Y. and Y.H.; supervision, Y.M., Z.L. and J.Z.; project administration, J.Y. and J.Z.; funding acquisition, J.Z., J.Y. and Y.M. All authors have read and agreed to the published version of the manuscript.

Funding: This research was funded by the National Natural Science Foundation of China (Grant No. U1906217, No. 42206177, No. 61890964), Shandong Provincial Natural Science Foundation (Grant No. ZR2022QD075), Fund of Technology Innovation Center for Ocean Telemetry, Ministry of Natural Resources (Grant No. 2022004), Qingdao Postdoctoral Application Research Project (Grant No. qdyy20210082), and the Fundamental Research Funds for the Central Universities (Grant No. 21CX06057A).

Data Availability Statement: The data used in this study are available on request from the first author.

Acknowledgments: We thank the China Marine Surveillance North Sea Aviation Detachment and Geospatial Data Cloud site, Computer Network Information Center, Chinese Academy of Sciences for providing AISA+ data and Hyperion data (<http://www.gscloud.cn> (accessed on 3 December 2020)). We would like to express our sincere appreciation to anonymous reviewers and editors who provided valuable comments to help improve this paper.

Conflicts of Interest: The authors declare no conflict of interest. The funders had no role in the design of the study; in the collection, analyses, or interpretation of data; in the writing of the manuscript, or in the decision to publish the results.

References

1. Kessler, J.D.; Valentine, D.L.; Redmond, M.C.; Du, M.; Chan, E.W.; Mendes, S.D.; Quiroz, E.W.; Villanueva, C.J.; Shusta, S.S.; Werra, L.M.; et al. A persistent oxygen anomaly reveals the fate of spilled methane in the Deep Gulf of Mexico. *Science* **2011**, *331*, 312–315. [[CrossRef](#)]
2. Zhong, Z.; You, F. Oil spill response planning with consideration of physicochemical evolution of the oil slick: A multiobjective optimization approach. *Comput. Chem. Eng.* **2011**, *35*, 1614–1630. [[CrossRef](#)]
3. Henkel, L.A.; Nevins, H.; Martin, M.; Sugarman, S.; Harvey, J.T.; Ziccardi, M.H. Chronic oiling of marine birds in California by natural petroleum seeps, shipwrecks, and other sources. *Mar. Pollut. Bull.* **2014**, *79*, 155–163. [[CrossRef](#)]
4. Berenshtein, I.; Paris, C.B.; Perlin, N.; Alloy, M.M.; Joye, S.B.; Murawski, S. Invisible oil beyond the Deepwater Horizon satellite footprint. *Sci. Adv.* **2020**, *6*, 8863. [[CrossRef](#)]
5. Wang, Y.B.; Du, P.P.; Liu, J.Q.; Chen, C.T. Spatial variation of coastal wetland vulnerability to oil spill stress in the Bohai Sea. *Front. Mar. Sci.* **2022**, *9*, 1073906. [[CrossRef](#)]
6. Guo, J.; Liu, X.; Xie, Q. Characteristics of the Bohai Sea oil spill and its impact on the Bohai Sea ecosystem. *Chin. Sci. Bull.* **2013**, *58*, 2276–2281. [[CrossRef](#)]
7. Li, Y.; Lan, G.X.; Liu, B.X. Oil spill information extraction with texture features HJ-CCD sensors: A case study in PL19-3 oil spill incident. *China Environ. Sci.* **2012**, *32*, 1514–1520.
8. Bao, M.; Zhang, J.; Zhang, X.; Meng, J.M. Oil spill detection from GF-1 images with spectral and textural features. *Adv. Mar. Sci.* **2020**, *38*, 504–512.
9. Huang, K.; Pan, Q.; Zhang, J.Y.; Wang, Y.L.; Yang, G.; Sun, W.W. Quantitative monitoring in oil spill incidents based on GF-1 satellite: Qingdao oil spill accident case. *Mar. Sci. Bull.* **2020**, *39*, 266–271.
10. Cally, C. Unique oil spill in East China Sea frustrates scientists. *Nature* **2018**, *554*, 17–18.
11. Lu, Y.C.; Liu, J.Q.; Ding, J.; Shi, J.; Chen, J.; Ye, X. Optical remote identification of spilled oils from the SANCHI oil tanker collision in the East China Sea. *China Sci. Bull.* **2019**, *6431*, 3213–3222.
12. Shen, Y.F.; Liu, J.Q.; Ding, J.; Jiao, J.N.; Sun, S.J.; Lu, Y.C. HY-1C COCTS and CZI observation of marine oil spills in the South China Sea. *J. Remote Sens.* **2020**, *24*, 933–944. [[CrossRef](#)]
13. Dai, Y.X.; Ma, Y.; Jiang, Z.C.; Du, K.; Wang, H.Q. Multi-spectral remote sensing detection of marine oil spill based on multi-kernel SVM decision fusion model. *Mari. Sci.* **2022**, *46*, 11–23.
14. An Average of One Oil Spill Incident Occurring Every Four Days along the Coast of China. Available online: <https://www.cnss.com.cn/old/25779.jhtml> (accessed on 17 August 2023).
15. Leifer, I.; Lehr, W.J.; Simecek-Beatty, D.; Bradley, E.; Clark, R.; Dennison, P.; Hu, Y.X.; Matheson, S.; Jones, C.E.; Holt, B.; et al. State of the art satellite and airborne marine oil spill remote sensing: Application to the BP deepwater horizon oil spill. *Remote Sens. Environ.* **2012**, *1249*, 185–209. [[CrossRef](#)]
16. Fingas, M.; Brown, C. Review of oil spill remote sensing. *Mar. Pollut. Bull.* **2014**, *831*, 9–23. [[CrossRef](#)] [[PubMed](#)]
17. Alpers, W.; Holt, B.; Zeng, K. Oil spill detection by imaging radars: Challenges and pitfalls. *Remote Sens. Environ.* **2017**, *201*, 133–147. [[CrossRef](#)]
18. Jatiault, R.; Dhont, D.; Loncke, L.; Dubucq, D. Monitoring of natural oil seepage in the Lower Congo Basin using SAR observations. *Remote Sens. Environ.* **2017**, *191*, 258–272. [[CrossRef](#)]
19. Mdakane, L.W.; Kleynhans, W. Feature selection and classification of oil spill from vessels using sentinel-1 wide-swath synthetic aperture radar data. *IEEE Geosci. Remote Sens. Lett.* **2020**, *19*, 4002505. [[CrossRef](#)]
20. Guo, G.; Liu, B.X.; Liu, C.Y. Thermal infrared spectral characteristics of bunker fuel oil to determine oil-film thickness and API. *J. Mar. Sci. Eng.* **2020**, *82*, 135. [[CrossRef](#)]
21. Hu, C.M.; Lu, Y.C.; Sun, S.J.; Liu, Y.X. Optical remote sensing of oil spills in the ocean: What is really possible? *J. Remote Sens.* **2021**, *2021*, 9141902. [[CrossRef](#)]
22. Ma, X.S.; Xu, J.G.; Wu, P.H.; Kong, P. Oil spill detection based on deep convolutional neural networks using polarimetric scattering information from sentinel-1 SAR images. *IEEE Trans. Geosci. Remote Sens.* **2021**, *60*, 4204713. [[CrossRef](#)]
23. Dong, Y.Z.; Liu, Y.X.; Hu, C.M.; MacDonald, I.R.; Lu, Y.C. Chronic oiling in global oceans. *Science* **2022**, *376*, 1300–1304. [[CrossRef](#)]
24. Hu, C.M.; Li, X.F.; Pichel, W.G.; Muller-Karger, F.E. Detection of natural oil slicks in the NW Gulf of Mexico using MODIS imagery. *Geophys. Res. Lett.* **2009**, *36*, L01604. [[CrossRef](#)]

25. Jing, Y.; An, J.B.; Liu, Z.X. A novel edge detection algorithm based on global minimization active contour model for oil slick infrared aerial image. *IEEE Trans. Geosci. Remote Sens.* **2011**, *49*, 2005–2013. [[CrossRef](#)]
26. Lu, Y.C.; Li, X.; Tian, Q.; Zheng, G.; Sun, S.J.; Liu, Y.X.; Yang, Q. Progress in marine oil spill optical remote sensing: Detected targets, spectral response characteristics, and theories. *Mar. Geod.* **2013**, *36*, 334–346. [[CrossRef](#)]
27. Lu, Y.C.; Hu, C.M.; Sun, S.J.; Zhang, M.W.; Zhou, Y.; Shi, J.; Wen, Y.S. Overview of optical remote sensing of marine oil spills and hydrocarbon seepage. *J. Remote Sens.* **2016**, *20*, 1259–1269.
28. Chen, Y.T.; Li, Y.Y.; Wang, J.S. An end-to-end oil-spill monitoring method for multisensory satellite images based on deep semantic segmentation. *Sensors* **2020**, *20*, 725. [[CrossRef](#)]
29. Lu, Y.C.; Shi, J.; Hu, C.M.; Zhang, M.W.; Sun, S.J.; Liu, Y.X. Optical interpretation of oil emulsions in the ocean—Part II: Applications to multi-band coarse-resolution imagery. *Remote Sens. Environ.* **2020**, *242*, 111778. [[CrossRef](#)]
30. Caillaud, K.; Roupioz, L.; Viallefont-Robinet, F. Modelling of the optical signature of oil slicks at sea for the analysis of multi- and hyperspectral VNIR-SWIR images. *Opt. Exp.* **2021**, *29*, 18224–18242. [[CrossRef](#)]
31. Cui, Y.Q.; Kong, D.M.; Zhang, X.D.; Kong, D.H.; Yuan, L. A method for estimating thick oil film on sea surface based on fluorescence signal. *Spectrosc. Spectr. Anal.* **2021**, *41*, 150–155.
32. Jiao, J.N.; Lu, Y.C.; Hu, C.M.; Shi, J.; Sun, S.J.; Liu, Y.X. Quantifying ocean surface oil thickness using thermal remote sensing. *Remote Sens. Environ.* **2021**, *2611*, 112513. [[CrossRef](#)]
33. Li, Y.C.; Liu, J.N.; Shi, H.D. Research on identification of marine oil spill based on polarization characteristics. *Acta Photon. Sin.* **2021**, *50*, 0712001.
34. Seydi, S.T.; Hasanlou, M.; Amani, M.; Huang, W.M. Oil spill detection based on multi-scale multi-dimensional residual CNN for optical remote sensing imagery. *IEEE J. Sel. Top. Appl. Earth Obs. Remote Sens.* **2021**, *14*, 10941–10952. [[CrossRef](#)]
35. Suo, Z.Y.; Lu, Y.C.; Liu, J.Q.; Ding, J.; Yin, D.Y.; Xu, F.F.; Jiao, J.N. Ultraviolet remote sensing of marine oil spills: A new approach of HaiYang-1C satellite. *Opt. Exp.* **2021**, *29*, 13486–13495. [[CrossRef](#)] [[PubMed](#)]
36. Yuan, L.; Wang, L.B.; Jiao, H.H. Research on estimation of oil-water ratio of light oil emulsion based on fluorescence spectroscopy. *Spectrosc. Spectr. Anal.* **2021**, *41*, 1852–1857.
37. Chen, Y.Q.; Yu, W.; Tang, J.Y.; Sun, Y.H.; Hu, H.S. A novel split-frequency feature fusion framework for processing the dual-optical images of offshore oil spills. *Mar. Pollut. Bull.* **2023**, *190*, 114840. [[CrossRef](#)] [[PubMed](#)]
38. Suo, Z.Y.; Li, L.; Lu, Y.C.; Liu, J.Q.; Ding, J.; Ju, W.M.; Li, M.C.; Yin, D.Y.; Xu, F.F. Sun glint reflectance facilitates performance of spaceborne UV sensor in oil spill detection. *Opt. Exp.* **2023**, *31*, 14651–14658. [[CrossRef](#)] [[PubMed](#)]
39. Cui, C.; Li, Y.; Liu, B.X.; Li, G.N.; Salehi, B.; Kainz, W. A new endmember preprocessing method for the hyperspectral unmixing of imagery containing marine oil spills. *ISPRS Int. J. Geo-Inf.* **2017**, *6*, 286. [[CrossRef](#)]
40. Zhu, X.; Li, Y.; Zhang, Q.; Liu, B. Oil film classification using deep learning-based hyperspectral remote sensing technology. *ISPRS Int. J. Geo-Inf.* **2019**, *8*, 181. [[CrossRef](#)]
41. Li, Y.; Lu, H.M.; Zhang, Z.D.; Liu, P. A novel nonlinear hyperspectral unmixing approach for images of oil spills at sea. *Int. J. Remote Sens.* **2020**, *41*, 46824699. [[CrossRef](#)]
42. Dilish, D. Spectral similarity algorithm-based image classification for oil spill mapping of hyperspectral datasets. *J. Spectr. Imag.* **2020**, *9*, a14.
43. Menezes, J.; Poojary, N. A fusion approach to classify hyperspectral oil spill data. *Multimed. Tools Appl.* **2020**, *79*, 5399–5418. [[CrossRef](#)]
44. Lu, Y.C.; Shi, J.; Wen, Y.S.; Hu, C.M.; Zhou, Y.; Sun, S.J.; Zhang, M.W.; Mao, Z.H.; Liu, Y.X. Optical interpretation of oil emulsions in the ocean—Part I: Laboratory measurements and proof-of-concept with AVIRIS observations. *Remote Sens. Environ.* **2019**, *230*, 111183. [[CrossRef](#)]
45. Yang, J.F.; Wan, J.H.; Ma, Y.; Zhang, J.; Hu, Y.B. Characterization analysis and identification of common marine oil spill types using hyperspectral remote sensing. *Int. J. Remote Sens.* **2020**, *41*, 7163–7185. [[CrossRef](#)]
46. Jiang, Z.C.; Zhang, J.; Ma, Y.; Mao, X.P. Hyperspectral remote sensing detection of marine oil spills using an adaptive long-term moment estimation optimizer. *Remote Sens.* **2021**, *141*, 157. [[CrossRef](#)]
47. Li, Y.; Yu, Q.; Xie, M.; Zhang, Z.D.; Ma, Z.J.; Cao, K. Identifying oil spill types based on remotely sensed reflectance spectra and multiple machine learning algorithms. *IEEE J. Sel. Top. Appl. Earth Obs. Remote Sens.* **2021**, *14*, 9071–9078. [[CrossRef](#)]
48. Yang, J.F.; Hu, Y.B.; Zhang, J.; Ma, Y.; Li, Z.W.; Jiang, Z.C. Identification of marine oil spill pollution using hyperspectral combined with thermal infrared remote sensing. *Front. Mar. Sci.* **2023**, *10*, 1135356. [[CrossRef](#)]
49. Lu, Y.C.; Tian, Q.J.; Wang, X.Y.; Zheng, G.; Li, X. Determining oil slick thickness using hyperspectral remote sensing in the Bohai Sea of China. *Int. J. Dig. Earth* **2013**, *6*, 76–93. [[CrossRef](#)]
50. Ren, G.B.; Guo, J.; Ma, Y.; Luo, X.D. Oil spill detection and slick thickness measurement via UAV hyperspectral imaging. *Haiyang Xuebao* **2019**, *41*, 146–158.
51. Jiang, Z.C.; Ma, Y.; Yang, J.F. Inversion of the thickness of crude oil film based on an OG-CNN model. *J. Mar. Sci. Eng.* **2020**, *8*, 653. [[CrossRef](#)]
52. Wang, M.Q.; Yang, J.F.; Liu, S.W.; Zhang, J.; Ma, Y.; Wan, J.H. Quantitative inversion ability analysis of oil film thickness using bright temperature difference based on thermal infrared remote sensing: A ground-based simulation experiment of marine oil spill. *Remote Sens.* **2023**, *15*, 2018. [[CrossRef](#)]

53. Yang, J.F.; Ma, Y.; Hu, Y.B.; Jiang, Z.C.; Zhang, J.; Wan, J.H.; Li, Z.W. Decision fusion of deep learning and shallow learning for marine oil spill detection. *Remote Sens.* **2022**, *14*, 666. [[CrossRef](#)]
54. Yang, J.F.; Wan, J.H.; Ma, Y.; Zhang, J.; Hu, Y.B.; Jiang, Z.C. Oil spill hyperspectral remote sensing detection based on DCNN with multi-scale features. *J. Coast. Res.* **2019**, *90*, 332–339. [[CrossRef](#)]
55. Du, K.; Ma, Y.; Jiang, Z.C.; Lu, X.Q.; Yang, J.F. Detection of Oil Spill based on CBF-CNN using HY-1C CZI Multispectral Images. *Acta Oceanol. Sini.* **2022**, *41*, 166–179. [[CrossRef](#)]
56. Zhong, Z.; Li, J.; Luo, Z.; Chapman, M. Spectral–spatial residual network for hyperspectral image classification: A 3-D deep learning framework. *IEEE Trans. Geosci. Remote Sens.* **2017**, *56*, 847–858. [[CrossRef](#)]
57. Ma, W.; Yang, Q.; Wu, Y.; Zhao, W.; Zhang, X. Double-branch multi-attention mechanism network for hyperspectral image classification. *Remote Sens.* **2019**, *11*, 1307. [[CrossRef](#)]
58. Li, R.; Zheng, S.; Duan, C.; Yang, Y.; Wang, X. Classification of hyperspectral image based on double-branch dual-attention mechanism network. *Remote Sens.* **2020**, *12*, 582. [[CrossRef](#)]
59. Shen, Y.; Zhu, S.; Chen, C.; Du, Q.; Xiao, L.; Chen, J.; Pan, D. Efficient deep learning of nonlocal features for hyperspectral image classification. *IEEE Trans. Geosci. Remote Sens.* **2020**, *59*, 6029–6043. [[CrossRef](#)]
60. Duan, P.H.; Lai, J.B.; Kang, J.; Kang, X.D.; Ghamisi, P.; Li, S.T. Texture-aware total variation-based removal of sun glint in hyperspectral images. *ISPRS J. Photog. Remote Sens.* **2020**, *166*, 359–372. [[CrossRef](#)]
61. Wang, B.; Shao, Q.F.; Song, D.M.; Li, Z.W.; Tang, Y.H.; Yang, C.L.; Wang, M.Y. A spectral-spatial features integrated network for hyperspectral detection of marine oil spill. *Remote Sens.* **2021**, *13*, 1568. [[CrossRef](#)]
62. Kang, X.D.; Deng, B.; Duan, P.H.; Wei, X.H.; Li, S.T. Self-supervised spectral-spatial transformer network for hyperspectral oil spill mapping. *IEEE Trans. Geosci. Remote Sens.* **2023**, *61*, 5507410. [[CrossRef](#)]
63. Wang, J.; Li, Z.W.; Yang, J.F.; Liu, S.W.; Zhang, J.; Li, S.B. A multilevel spatial and spectral feature extraction network for marine oil spill monitoring using airborne hyperspectral image. *Remote Sens.* **2023**, *15*, 1302. [[CrossRef](#)]
64. Qin, A.Y.; Shang, Z.W.; Tian, J.Y.; Wang, Y.L.; Zhang, T.P. Spectral–spatial graph convolutional networks for semisupervised hyperspectral image classification. *IEEE Geosci. Remote Sens. Lett.* **2019**, *16*, 241–245. [[CrossRef](#)]
65. Liu, Q.C.; Xiao, L.; Yang, J.X.; Wei, Z.H. CNN-enhanced graph convolutional network with pixel- and superpixel-level feature fusion for hyperspectral image classification. *IEEE Trans. Geosci. Remote Sens.* **2020**, *59*, 8657–8671. [[CrossRef](#)]

Disclaimer/Publisher’s Note: The statements, opinions and data contained in all publications are solely those of the individual author(s) and contributor(s) and not of MDPI and/or the editor(s). MDPI and/or the editor(s) disclaim responsibility for any injury to people or property resulting from any ideas, methods, instructions or products referred to in the content.